CHEMISTRY OF MATERIALS
ARTICLE
pubs.acs.org/cm

Multiwavelength Luminescence in Lanthanide-Doped Hydrocalumite and Mayenite

Marta Domínguez,[†] María Elena Pérez-Bernal,[†] Ricardo Jesús Ruano-Casero,[†] Cristobalina Barriga,[‡] Vicente Rives,[*,†] Rute A. S. Ferreira,[§] Luís D. Carlos,[§] and João Rocha[∥]

[†]GIR-QUESCAT, Departamento de Química Inorgánica, Universidad de Salamanca, Salamanca, Spain
[‡]Departamento de Química Inorgánica e Ingeniería Química, Universidad de Córdoba, Córdoba, Spain
[§]Department of Physics and [∥]Department of Chemistry, CICECO, University of Aveiro, 3810-193 Aveiro, Portugal

ABSTRACT: Lanthanide (Eu and Nd)-doped hydrocalumite has been prepared by a coprecipitation method. All samples, with Eu^{3+} and Nd^{3+} contents up to 4% (molar ratio), show a single crystallographic phase, without segregation of secondary lanthanide-containing phases. Calcination affords lime and mayenite, with lanthanide cations embedded in the structure. The photoluminescence spectra of the noncalcined samples consist of Eu^{3+} (in the visible region) and Nd^{3+} (in the NIR) intra-4f transitions and a broad band ascribed to Al-related defects. The Eu^{3+} $^5D_0$ lifetime values and quantum efficiency of the Eu^{3+}/Nd^{3+} codoped hydrocalumite decrease ca. 10%, relative to the single doped material, suggesting that the Nd^{3+} incorporation activates nonradiative channels for the $^5D_0$ depopulation. High-temperature stable ceramic pigments, prepared from Eu^{3+} and Nd^{3+} doped hydrocalumite precursors, afford multiwavelength luminescent materials emitting in a large vis/NIR spectral region, with potential applications as barcodes and in broadband amplifiers. The emission spectra of the calcined samples give unequivocal evidence for the presence of two Eu^{3+} local environments, attributed to Eu^{3+} sites in CaO and mayenite. Upon calcination, the absolute emission quantum yield of the Eu^{3+}-doped sample increases from less than 0.01 to 0.06.

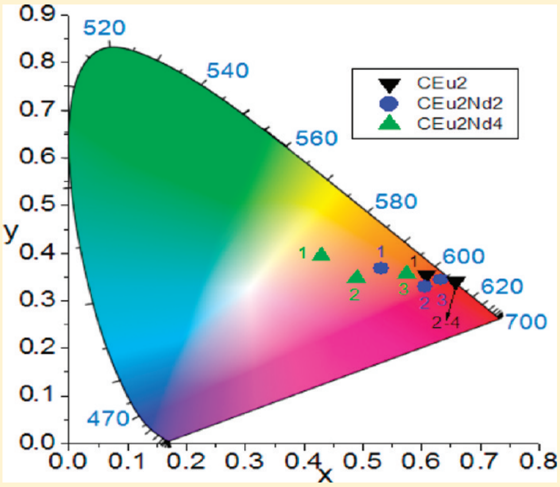

KEYWORDS: multiwavelength luminescence, hydrocalumite, mayenite, lanthanide doping

INTRODUCTION

Layered double hydroxides (LDHs) have deserved much attention in the last two decades. These natural and synthetic solids exhibit a layered structure similar to that of brucite, $Mg(OH)_2$, but with a partial Mg^{2+}/M^{3+} substitution ($M^{3+} = Al^{3+}$ in natural hydrotalcite), the positive charge in excess being balanced by intercalated hydrated anions. Their chemical composition can be varied in a broad range, concerning both the nature of the brucite-like layers (usually M^{2+} and M^{3+}, although compounds containing cations with other formal charges are also known) and interlayer anions. Their properties have been reviewed by different authors[1−9] and have been applied in a broad range of fields, namely, catalyst precursors and catalyst supports,[1,10−13] antacids and drugs support for controlled delivery,[14−17] anion scavengers for water purification,[18,19] composites,[20,21] especially upon delamination of the layers,[22] and so forth. Because calcination of LDHs produces homogeneously dispersed mixed oxides, they have also been tested as a precursor for ceramic pigments.[23−27]

Several papers have dealt with LDHs containing lanthanides, mainly looking for an improvement in their color or luminescent properties. Although in most cases the lanthanide has been incorporated as an anionic coordination compound in the interlayer space of the LDH,[28−30] a few reports are available on the incorporation of the lanthanide cation in the brucite-like layers.[31−33] The ionic radii of the trivalent lanthanide cations, however, are usually too large to be hosted in the octahedral holes of the brucite-like layers and, as a result, strong structural distortions occur. In fact, when the lanthanide ions have been incorporated in the brucite-like layers only a partial Al^{3+}/Ln^{3+} substitution was attained, and pure Mg^{2+}/Ln^{3+} compounds never formed. Other lanthanide-containing layered systems have been also studied,[34,35] and the subject has been recently reviewed by Carlos et al.[36]

The size of the octahedra in the brucite-like layers is, to a certain extent, controlled by the size of the divalent cation. For stability reasons, the molar M^{2+}/M^{3+} ratio should be always larger than one and ideally larger than two. Consequently, an alternative way to incorporate *large* lanthanide cations in the brucite-like layers is to substitute Ca^{2+} (ionic radius in octahedral cordination 1.14 Å) for Mg^{2+} (0.86 Å). Because the ionic radii of Ln^{3+} cations in octahedral coordination range between 1.17 Å (La^{3+}) and 1.00 Å (Lu^{3+}), structurally stable solids would then be formed.

Received: February 8, 2011
Revised: February 10, 2011
Published: March 02, 2011

Hydrocalumite, or Friedel's salt, is a layered material with the chemical formula $Ca_2Al(OH)_6Cl\cdot 2H_2O$ and Ca^{2+} and Al^{3+} cations hepta- and hexa-coordinated, respectively. Substitution of larger cations (e.g., Sc^{3+}) for Al^{3+} gives rise to an increase in the lattice parameter a and a decrease in the parameter c.[37]

Calcination of hydrocalumite gives rise to a mixture of mayenite, $Ca_{12}Al_{14}O_{33}$, a phase commonly found in concrete, and CaO (as mentioned above, the molar Ca^{2+}/Al^{3+} ratio in hydrocalumite is equal to 2 and, thus, pure mayenite cannot be formed upon calcination). In the cubic structure, Al^{3+} ions are tetrahedrally coordinated by oxide anions while the Ca^{2+} cations are hepta-coordinated.[38] Mayenite also has been recently used as a base catalyst for metanolysis of sunflower oil,[39] and it has received much attention as a room-temperature-stable electrode.[40,41]

The main interest for incorporating lanthanide cations into a LDH phase is that the properties of LDHs can be tuned by varying the host and/or guest composition and the interaction between the two. Some of the papers cited above are good examples of the optical properties of these layered materials containing lanthanide cations.[36]

Our approach is slightly different as we aim to study not the parent LDH materials but the solids calcined at high temperatures, as they would be in the case of ceramic pigments. This study consists of the preparation of pristine hydrocalumite (containing exclusively Ca^{2+} and Al^{3+}) doped with different amounts of Eu^{3+} and Nd^{3+}. Luminescent materials doped with Eu^{3+} usually exhibit intense emission bands due to electronic transitions from the $^5D_0$ first excited state to the fundamental $^7F_{0-4}$ manifold.

Our aim is the preparation of high-temperature stable ceramic pigments, starting from LDH-type materials. Our choice has been hydrocalumite, where the presence of voluminous Ca^{2+} cations permits incorporation of rather large lanthanide cations without developing strong stresses in the crystal. The LDH structure has proved to be adequate to yield structural pigments without the use of mineralizers and not requiring very high calcination temperatures.[24−27] For the first time, to the best of our knowledge, codoping of LDHs with Eu^{3+} and Nd^{3+} ions affords luminescent materials emitting in a large spectral region covering almost the entire visible (vis) and a significant part of the NIR regions. Multiwavelength luminescent materials in the vis/NIR ranges may have potential applications as barcodes[42] and broadband amplifiers for the development of ultrabroadband wavelength-division-multiplexing (WDM) network.[43]

■ EXPERIMENTAL SECTION

Samples Preparation. For preparing the starting compound we used Ca^{2+} and Al^{3+} chlorides from Panreac, Nd^{3+} chloride from Aldrich, and Eu^{3+} oxide from BDH Chemicals; gases were from L'Air Liquide (Spain). The samples were prepared by coprecipitation at room temperature and constant pH. To avoid precipitation of $CaCO_3$, water to prepare the solutions and to wash the precipitates had been previously boiled and cooled while flowing nitrogen. Solution A was prepared by dissolving 18.6 mg of NaOH in 150 mL of water; solution B (for pH control) was prepared by dissolving 80 g of NaOH in 1 L of water, and solution C was prepared by dissolving the required amounts of $CaCl_2\cdot 2H_2O$ and $AlCl_3\cdot 6H_2O$ in 75 mL of water, to obtain solids with the required Ca/Al/Eu/Nd molar ratios. Eu_2O_3 was dissolved with a few drops of concentrated HCl acid. The method was as follows:

Solution A was placed in a three-necked, 1 L, round-bottom flask; solution C was added from a compensated pressure funnel; and solution B was used to maintain a constant pH (11.5 ± 0.1) with a Dosimat Metrohm instrument coupled to a Metrohm pHmeter; the pH electrode and the funnel for addition of the basic solution were connected through two necks of the round-bottom flask, and the remaining neck was used to flow continuously nitrogen to avoid contamination by atmospheric CO_2. The liquid and the suspension formed were stirred magnetically (Agimatic-N P from Selecta). Solution C was dropwise added onto solution A, giving rise to a milky suspension; once addition was complete, the suspension was aged at room temperature under N_2 flow and magnetic stirring for 48 h. The suspension was filtered with a water pump in a Büchner funnel, and the solid was washed four times with 50 mL portions of decarbonated water. The powder was then stored in a desiccator for 24 h and finally dried in an oven at open air at 60 °C. The pH of the mother liquor was in the 11.2−11.9 range and that for the washing liquids in the 11.1−11.8 range. Approximately 12 g of solid was obtained in each case, resulting a yield close to 100%. Actually, only <70 ppm Al and <1000 ppm Ca were detected in the mother liquor.

While keeping a Ca/trivalent cation molar ratio close to 2, the Eu content was varied to values representing 0, 1, and 2% with respect to Al, and the Eu/Nd ratio was varied from 1/1 to 1/4, giving rise to a total of seven samples, six of them containing lanthanide ions. Ca2Al1 stands for the lanthanide-free sample, while EuX will stand for a given sample where X% of Al^{3+} have been substituted by Eu^{3+} and EuXNdY for a sample containing, in addition, Nd^{3+} cations, for which the molar percentage, with respect to Al^{3+}, corresponds to Y.

The samples were calcined up to 1300 °C at a heating rate of 5 °C/min with a retention time of 5 h, to prepare oxides with the mayenite structure. The calcined samples are named as C-YYY, where YYY stands for the symbol of the uncalcined sample.

Characterization. *Element Chemical Analysis.* Ca, Al, Eu, and Nd contents were determined at Servicio General de Análisis Químico Aplicado (Universidad de Salamanca, Spain) in a plasma emission spectrometer ICP-PES from Jobin Yvon, model Ultima II, after digestion of the samples in nitric acid in a Ethos Sel microwave oven from Milestone. Chlorine was determined by the Volhard method.

Powder X-ray Diffraction. The powder X-ray diffraction (PXRD) diagrams were recorded on a Siemens D-500 instrument equipped with a Difract-AT and DACO-MP microprocessor with Cu Kα radiation (λ = 1.54 Å) with a current of 30 mA and an acceleration voltage of 40 kV; the 5−70° (2θ) range was scanned at a speed of 2°/min and set time of 1.5 s. The crystalline phases were identified by comparing the diffraction diagrams with standards (JCPDS) and literature data. Lattice parameters were obtained by refinement using the AFFMA least-squares program.[44]

Thermal Analyses. Thermogravimetric analysis and differential thermal analysis were carried out simultaneously on the same portion of sample on SDT Q600 TGA-DTA equipment from TA Universal Analysis. The instrument also permits the derivative thermogravimetric curve (DTG) to be plotted. Analysis of evolved gases (EGA) was carried out by connecting the exit of the thermal equipment to Pfeiffer Vacuum ThermoStar TG-MS equipment. The analyses were carried out under dynamic oxygen or helium, at a heating rate of 10 °C/min, up to 1300 °C.

Fourier Transform Infrared Spectroscopy. The FT-IR spectra of the samples were recorded by the KBr pellet technique in a Perkin-Elmer FT-IR 1600 instrument. One hundred spectra were recorded with a nominal resolution of 4 cm^{-1}, to improve the signal-to-noise ratio.

Specific Surface Area and Porosity. The specific surface area and porosity of the samples were determined from the adsorption−desorption nitrogen isotherms at −196 °C with an automatic volumetric instrument ASAP 2000 from Micromeritics. About 200 mg of sample was used, which was degassed at room temperature for 20 h and then at 110 °C for 5 h to remove weakly adsorbed species. The BET equation was used to determine the specific surface area, and porosity was determined using the Cranston and Inkley method; the thickness of the adsorbed layer was determined by using the Halsey equation, and the presence of microporosity and the external surface area were determined from the t-plots.

Scanning Electron Microscopy. The SEM micrographs were obtained in a JEOL 6300 instrument at 25 kV by deposition of a drop of sample suspension on a Cu sample holder and covered with Au layer by sputtering in a Baltec SCD005 apparatus.

Color Coordinates. Body color of the samples was quantified by using a Konica Minolta colorimeter (Chroma Meter CR 400 model), equipped with a pulsed xenon lamp. The data were collected by a personal computer through a RS-232 interface and were analyzed with Color Data CM-100W Spectra Magic NX software. We used the $L^*a^*b^*$ system (also known as CIELAB) as the color space, where L^* stands for lightness (ranging from $L^* = 0$ for black to $L^* = 100$ for white), and a^* and b^* are chromaticity coordinates, where negative values for a^* indicate green and positive values indicate red, while negative values for b^* indicate blue and positive values indicate yellow. Three measurements (with three twinkles each) on three different spots were taken for each sample, averaging the results. Samples were placed between flat colorless glasses on a black sample holder. The instrument had been previously calibrated with Minolta white reference CR-A43 (XYZ parameters 0.3133, 93.80, and 0.3194, respectively).

Photoluminescence. The photoluminescence spectra in the near-infrared (NIR) and in the ultraviolet/visible (UV/vis) spectral ranges were recorded at 10 K and room temperature with a modular double grating excitation spectrofluorometer with a TRIAX 320 emission monochromator (Fluorolog-3, Horiba Scientific) coupled to a H9170-75 Hamamatsu photomultiplier and to a R928 Hamamatsu photomultiplier, respectively. The spectra were acquired using the front face mode and were corrected for detection and optical spectral response. Emission was corrected for the spectral response of the monochromators and the detector using the typical correction spectrum provided by the manufacturer, and the excitation spectra were corrected for the spectral distribution of the lamp intensity using a photodiode reference detector. The time-resolved emission features and lifetime measurements in the 10^{-6}–10^{-3} s time range were acquired at 10 K and room temperature with the setup described for the UV/vis photoluminescence spectra using a pulsed Xe–Hg lamp (6 μs pulse at half width and 20–30 μs tail). The room temperature emission decay curves in the 10^{-9} s time scale were recorded on a spectrofluorometer (Fluorolog TCSPC, Horiba Scientific) coupled to a TBX-04 photomultiplier tube module (950 V), 200 ns time-to-amplitude converter. The exciting source was a Horiba-Jobin-Yvon pulsed diode (NanoLED-390, peak at 330 nm, 1.2 ns pulse duration, 1 MHz repetition rate, and 150 ns synchronization delay). The experimental excitation pulse was measured using a LUDOX scattering solution in water. The emission color coordinates for the calcined samples were calculated accordingly to the Commission Internationale d'Eclairage (CIE) method described for the 2° standard observer.

Absolute Emission Quantum Yields. The absolute emission quantum yields were measured at room temperature using a quantum yield measurement system C9920-02 from Hamamatsu with a 150 W xenon lamp coupled to a monochromator for wavelength discrimination, an integrating sphere as sample chamber, and a multi-channel analyzer for signal detection. Three measurements were made for each sample so that the average value is reported. The method is accurate to within 10%.

RESULTS AND DISCUSSION

Characterization. Element chemical analysis results are summarized in Table 1. In all cases we aimed to prepare samples with a M^{2+}/M^{3+} molar ratio of 2.0, and the values reported here are close to this value. The expected Ca/Cl molar ratio for hydrocalumite is 2.0, and the experimental values are roughly coincident, although somewhat lower in all cases.

All samples were white, with luminosity (ΔL^*) values of 26 ± 1, while chromatic coordinates Δa^* and Δb^* were close to zero (always in the +1/−1 range). A slight decrease in coordinate Δb^* was observed as the Nd content was increased. The color difference ΔE^* was always in the 25–28 range. Calcination at 1300 °C led to a slight darkening of the samples, ΔL^* now being in the 14–21 range. For the calcined samples, incorporation of Eu gives rise to a minor increase in chromatic parameter Δa^* (red), which is enhanced when Nd^{3+} is simultaneously added; parameter Δb^* decreases. Color differences for the calcined samples are much more important than for the uncalcined ones, ΔE^* ranging from 27 for sample Ca2Al1 to 25 for sample Eu1Nd4 and 21 for sample Eu2Nd4.

Table 1. Element Chemical Analysis and Some Molar Ratios for the Samples Prepared[a]

sample	Ca[b]	Al[b]	Eu[b]	Nd[b]	Cl[b]	Ca/M^{3+}[c]	Eu/Al[c]	Nd/Eu[c]	Ca/Cl[c]
Ca2Al1	28.62	9.57			13.09	2.01			1.93
Eu1	28.68	9.44	0.71		15.53	2.02	0.013		1.63
Eu1Nd2	28.30	9.29	0.58	1.10	13.99	1.98	0.011	2.00	1.79
Eu1Nd4	26.38	8.96	0.60	2.09	13.11	1.88	0.012	3.67	1.81
Eu2	29.03	9.22	0.90		13.53	2.07	0.017		1.90
Eu2Nd2	29.07	9.08	1.07	0.97	14.38	1.96	0.021	0.95	1.79
Eu2Nd4	27.84	9.09	0.90	1.85	13.19	2.08	0.018	2.11	1.87

[a] Values have been rounded. [b] Mass percentage. [c] Molar ratio.

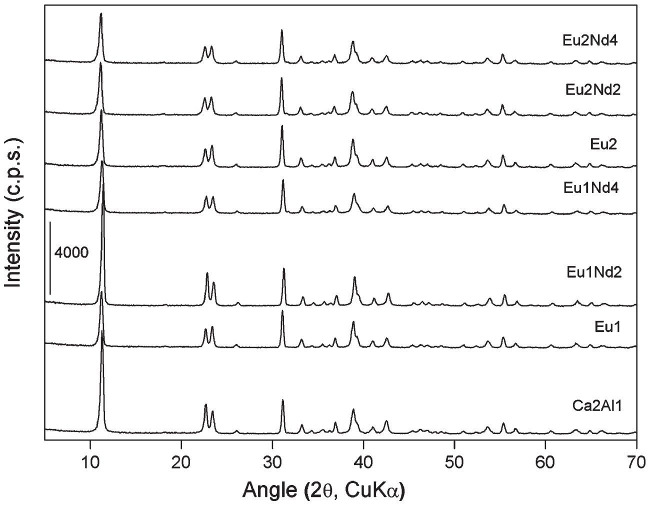

Figure 1. Powder X-ray diffraction (PXRD) diagrams of the samples prepared.

The PXRD patterns of all seven samples (Figure 1) are very similar, although small differences in the relative intensities of the reflections are observed. No secondary phases ascribed to other Ca-, Al-, Eu-, and Nd-containing compounds are detected, suggesting that the Ln^{3+} cations are located within the hydrocalumite structure, isomorphically substituting the cations in original hydrocalumite. The patterns correspond to that of hydrocalumite in the JCPDS files (file 35-0105). The lattice parameters c and a (46.95 and 5.74 Å, respectively, for hydrocalumite, JCPDS file 35-0105) have been determined using literature equations,[45] and the crystallite size, D, has been determined using the Scherrer's formula.[46,47] We have used in both cases the most intense diffraction peak, due to planes (006), recorded close to $2\theta = 11°$. The values determined are summarized in Table 2. Experimental broadening (0.2321°) was experimentally determined using LaB_6 as the reference. Within experimental error, no variation is observed in the lattice parameters. The crystallite sizes are in the 340–570 Å range, with no systematic

Table 2. Lattice Parameters (c and a, in Å) and Crystallite Size (D, in Å) of the Samples Prepared along with Standard Deviation (SD)

sample	c	SD	a	SD	D
Ca2Al1	46.95	0.02	5.742	0.002	440
Eu1	46.85	0.02	5.734	0.002	380
Eu1Nd2	46.73	0.03	5.727	0.002	570
Eu1Nd4	46.83	0.02	5.734	0.002	380
Eu2	46.91	0.08	5.746	0.005	430
Eu2Nd2	47.05	0.04	5.75	0.02	360
Eu2Nd4	47.00	0.03	5.75	0.02	340

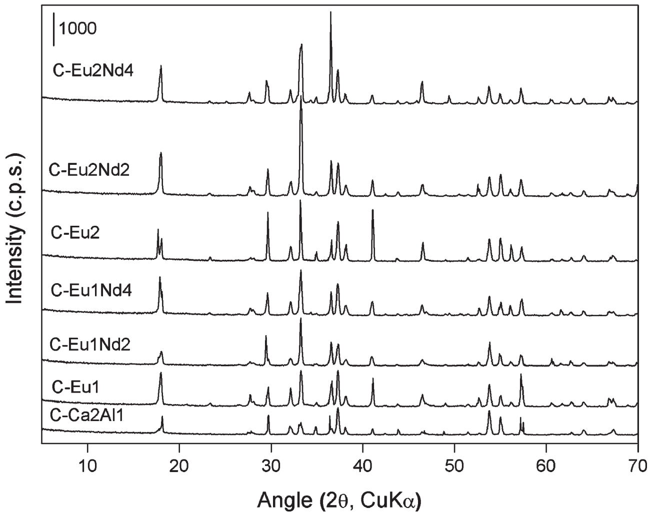

Figure 2. Powder X-ray diffraction diagrams of the calcined solids.

change with the lanthanide content. The ionic radius of Al^{3+} is 0.53 Å (tetrahedral coordination) or 0.68 Å (octahedral coordination),[48] while for Ca^{2+} it ranges from 1.14 to 1.32 Å on passing from hexa- to nona-coordination, and similar values have been reported[47] for Eu^{3+} and Nd^{3+} cations. It is then obvious that Al^{3+}/Ln^{3+} isomorphical substitution would give rise to larger distortions than the Ca^{2+}/Al^{3+} substitution; unfortunately, the experimental techniques available to us did not permit us to fix this point. On the other hand, no segregation of new crystalline phases containing Eu or Nd is observed, presumably because the lanthanide cations isomorphically substitute the cations in the parent hydrocalumite structure. In a previous study[34] on Mg, Al, and Y hydrotalcites it has been reported that structural distortions, giving rise to broader diffraction maxima, were observed only when the yttrium content reached values much larger than those reported here for the lanthanide cations. Distortions were not observed, however, in Mg, Al, Cr, and Y hydrotalcites with Y content of the same order as those of Eu and Nd here existing.[25]

The PXRD patterns of the calcined solids are included in Figure 2. The peaks recorded correspond exclusively to crystalline phases of mayenite and calcium oxide (JCPDS files 48-1882 and 37-1497, respectively). The Ca/Al ratio in the original hydrocalumite sample was roughly equal to 2, while such a ratio is 12/14 in mayenite, and consequently segregation of CaO takes place.

Table 3. Lattice Parameter (a, in Å) and Crystallite Size (D, in Å) of the Calcined Samples along with Standard Deviation (SD)

	Mayenite			CaO		
Sample	a	SD	D	a	SD	D
C-Ca2Al1	12.019	0.005	380	4.813	0.002	430
C-Eu1	12.019	0.005	420	4.815	0.001	430
C-Eu1Nd2	12.035	0.003	460	4.816	0.002	370
C-Eu1Nd4	12.032	0.003	390	4.814	0.002	370
C-Eu2	12.023	0.002	420	4.814	0.001	380
C-Eu2Nd2	12.029	0.002	410	4.815	0.001	380
C-Eu2Nd4	12.039	0.002	410	4.814	0.002	390

The relative intensities of the diffraction maxima somewhat change in some cases with respect to the values for the reference compound. In this case, the lattice parameter for both phases (mayenite and calcium oxide) has been calculated using the equation for cubic structures.[45]

The lattice parameter and crystallite size values for all calcined solids are summarized in Table 3. The lattice parameter for the CaO phase is always the same, in the presence or absence of lanthanide cations. However, some variations are observed in the values of the lattice parameter of the mayenite phase. The parameter increases slightly upon incorporation of Eu^{3+} or Nd^{3+}, keeping always a value larger than for the lanthanide-free sample. The crystallite sizes change randomly, with no evident relationship with the chemical composition of the precursor.

The intensities of the diffraction maxima corresponding to mayenite change from phase to phase, and minor shifts are observed. In contrast, the maxima due to CaO are recorded always in the expected positions, and in addition, their relative intensities coincide with those reported in the JCPDS file for this compound. As no separate phases corresponding to Eu or Nd oxides are identified, we conclude that these cations are incorporated exclusively in the mayenite phase.

Thermal analysis curves recorded in flowing He or oxygen are also similar for all compounds prepared. The TG-DTG curves for the original Ca2Al1 sample are included in Figure 3. Gases evolved during thermal decomposition have been analyzed by mass spectrometry (MS), following the intensities of the signals due to $m/z = 35$ and 36 (for chlorine or HCl) and 17 and 18 (for water vapor). Total mass loss was in the range 39−42% for all samples. Decomposition takes place in four steps. According to the MS results, the first two steps (with maximum mass loss rates at ca. 120 and 310 °C, corresponding respectively to mass losses of 13 and 16%) correspond to the removal of water vapor, and the last mass loss (8%) above 1000 °C corresponds to the removal of HCl. The precise nature of the vapors or gases evolved around 700 °C, amounting to ca. 3% of the initial sample mass, could not be determined: it did not correspond to water and could be due to some chlorine-containing species. In other words, chlorine is evolved in two consecutive steps at medium and high temperatures.

PXRD analysis of the residues of the calcination at different temperatures was also carried out. At 500 °C (i.e., after the second mass loss and before the weak third one) only an amorphous phase was identified. The residue of the calcination at 900 °C showed diffraction maxima due to mayenite and CaO and also some minor maxima due to Ca(OH)Cl. The diagrams are included in Figure 4.

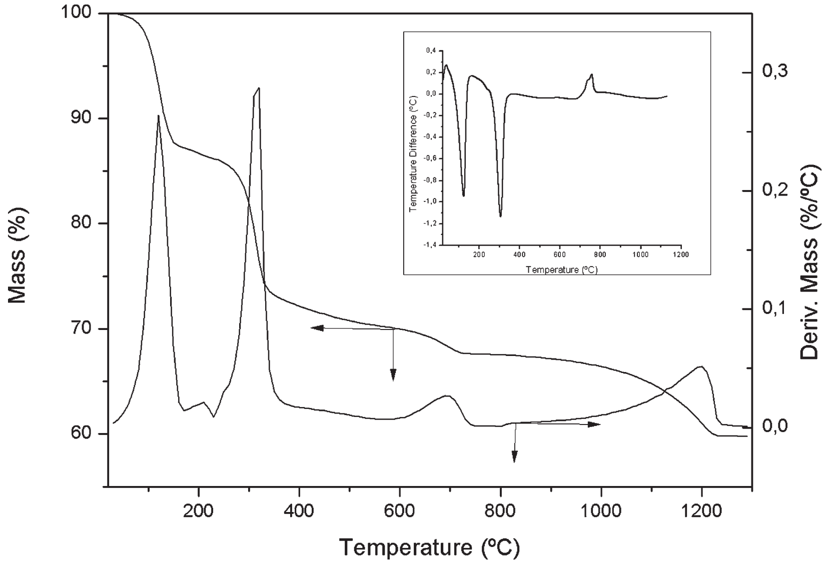

Figure 3. Thermogravimetric (TG) and derivative thermogravimetric (DTG) analyses curves of the original Ca2Al1 sample. The inset shows the differential thermal analysis (DTA) curve of sample Eu2Nd4.

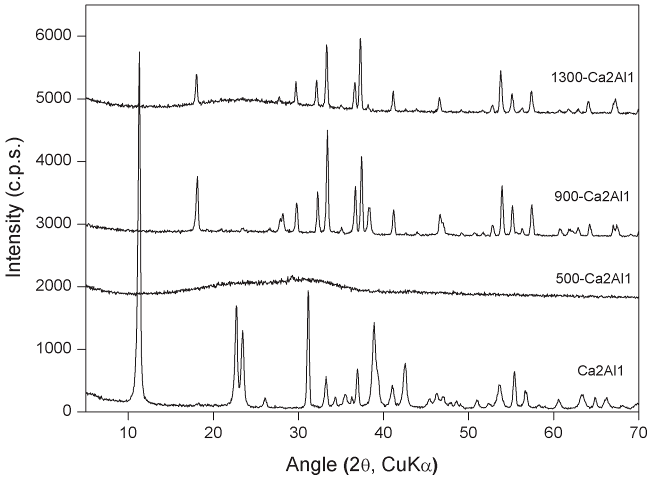

Figure 4. Powder X-ray diffraction diagrams of sample Ca2Al1 and the residues obtained after its calcination at 500 (500-Ca2Al1), 900 (900-Ca2Al1), and 1300 °C (1300-Ca2Al1).

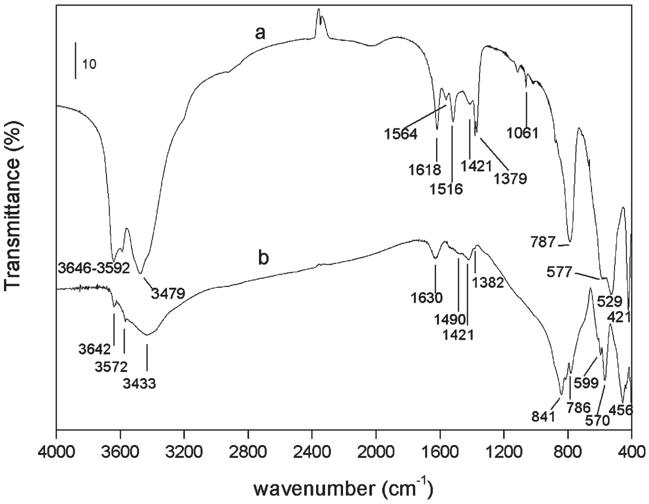

Figure 5. FT-IR spectra of (a) original sample Ca2Al1 and (b) after calcination at 1300 °C.

On these grounds, decomposition can take place through the following steps (numbers on the right stand for the calculated mass losses associated to the reactions shown):

$$\begin{array}{llll}
14\ Ca_2Al(OH)_6Cl\cdot 2H_2O & \rightarrow & 14\ Ca_2Al(OH)_6Cl + 28\ H_2O & 12.83 \\
14\ Ca_2Al(OH)_6Cl & \rightarrow & 7\ [2Ca(OH)Cl + 2CaO + Al_2O_3] + 35\ H_2O & 16.03 \\
7\ [2Ca(OH)Cl + 2CaO + Al_2O_3] & \rightarrow & Ca_{12}Al_{14}O_{33} + 16\ CaO + 14\ HCl & 13.00 \\
\hline
14\ [Ca_2Al(OH)_6Cl\cdot 2H_2O] & \rightarrow & Ca_{12}Al_{14}O_{33} + 16\ CaO + 14\ HCl + 63\ H_2O & 41.86
\end{array}$$

The calculated values and those experimentally measured are the same, within experimental error, assuming the third and fourth steps as a single one, because the amorphous nature of the solid formed at 500 °C makes it impossible to determine the precise nature of the species formed.

The curves are essentially identical for all samples, as the low percentage of lanthanide cations gives rise to differences in mass loss that can be even within the experimental error.

All DTA curves were very similar (see data for sample Eu2Nd4 in Figure 3, inset) and consist of two strong endothermic effects, coinciding with the main mass losses due to evolution of water vapor, and two much weaker exothermic effects which roughly coincide with the third and fourth mass losses. Except for combustion processes (releasing energy and with a mass decrease), other mass loss processes usually take place with absorption of energy (endothermic DTA signals). Consequently, we should conclude that the third and fourth thermal effects are the result of the superposition of an endothermic effect (due to mass loss, as seen from the TG curves) and an exothermic one (crystallization of new phases). The exothermic effect is recorded as a single signal for sample Ca2Al1. However, upon incorporation of the lanthanide ions, the maximum shifts toward lower temperatures by ca. 50 °C, splitting simultaneously into two signals. These results confirm that the exothermic process corresponds to the collapse of the layered structure. The probably weak structural distortions arising from incorporation of the lanthanide cations in some sort of way assist decomposition of the layered structure at lower temperatures.

The FT-IR spectrum of sample Ca2Al1 is included in Figure 5a. The broad band centered around 3650 cm^{-1} is due to the stretching mode of hydroxyl groups, both from the layers and of interlayer water molecules,[49,50] broadening arising from hydrogen bonding existing between these species. In addition, there is a sharp shoulder at 3646 cm^{-1} with a much weaker shoulder at 3592 cm^{-1} ascribed to the stretching mode of OH groups bonded to Ca^{2+} cations. The bands due to metal—OH bonds are recorded in the low wavenumbers region, 787, 577, and 529 cm^{-1}. The doublet close to 2350 cm^{-1} is due to a miscancellation of the CO_2 bands because of a different concentration of CO_2 in the atmosphere when recording the background and the spectrum of the sample.

It should be noticed that, in addition, several bands are recorded in the medium range of the spectrum. The band at 1618 cm^{-1} is due to the deformation mode of water molecules,[49,50] and the other weak bands are due to surface carbonate or hydrogen carbonate species formed by adsorption of atmospheric CO_2 on the external surface of the crystallites during handling to record the spectrum. It should be recalled that, according to elemental chemical analysis, carbonate was absent in the sample, as cautions were taken during synthesis to avoid any contact of the solutions with atmospheric CO_2. Moreover, if such cautions are not taken, precipitation of $CaCO_3$ is hardly avoided, and no evidence of $CaCO_3$ was concluded from PXRD analysis. Consequently, the carbonate species should be merely adsorbed on the surface of the crystallites and not in the interlayer space of the solid, thus also accounting for the relative weakness of these bands.

On calcination at 1300 °C the spectrum shows some important changes, Figure 5b. Again a broad but less intense band is recorded around 3500 cm^{-1}, due to the stretching mode of the hydroxyl groups probably adsorbed on the external surface of the crystallites, as the PXRD pattern for the calcined solid corresponded exclusively to non-hydroxylated mayenite and CaO. The sharp shoulders in the high wavenumbers region are due to the stretching mode of OH groups linked to Ca^{2+} cations in the two crystallographic phases identified. The central section of the spectrum again shows bands due to the deformation mode of water molecules and some weak sharp bands originated by carbonate and/or hydrogencarbonate species, although these species should be different from those existing in hydrocalumite, as concluded from the different relative intensities of the bands in this region. The main differences are found in the low wavenumbers region, where lattice vibrations are recorded, due to the major changes originated by the phase transformations: the spectrum is dominated by a strong band at 841 cm^{-1}, absent in the spectrum of hydrocalumite, and a sharp band at 570 cm^{-1}. These are due to metal—oxygen bonds.

The spectra for the lanthanide-containing samples are very similar to that of sample Ca2Al1, the main differences being the change in the relative intensities of the carbonate-related bands, probably because of minor changes in the surface acidity of the samples upon incorporation of Eu^{3+} and Nd^{3+}.

The BET specific surface area of the samples, as determined by the method, the external surface area and the surface area equivalent to adsorption in micropores (both determined by the *t*-plot method[51,52]), and the micropore volume for all samples, are given in Table 4. Incorporation of lanthanide cations gives rise to the development of microporosity, especially for the samples with a larger Eu content, and the specific surface area also increases. For a given Eu content, when the amount of Nd increases, an important surface area development is observed. Microporosity cannot be related to adsorption of nitrogen molecules in the interlayer space, as, because of their dynamic diameter and the height of the interlayer space, they cannot access the interlayer zone of the crystals. If we assume, however, that the lanthanide cations isomorphically substitute some cations in the hydrocalumite lattice, development of microporosity can be only related to changes in the formation or aggregation of the crystals during the preparation process, probably because of the different acidity due to the presence of the lanthanide cations. Calcination at 1300 °C gives rise to extremely compact solids for which the specific surface areas measured are below the detection limit of the equipment used.

Table 4. Surface Texture Properties of the Samples

sample	S_{BET}[a]	S_t[a]	S_{mp}[a]	V_{mp}[b]
Ca2Al1	12	14		
Eu1	11	9	2	1.1
Eu1Nd2	11	9	3	1.5
Eu1Nd4	26	23	3	1.6
Eu2	18	13	5	2.5
Eu2Nd2	19	14	5	2.2
Eu2Nd4	27	22	5	2.3

[a] m^2/g. [b] mL/g.

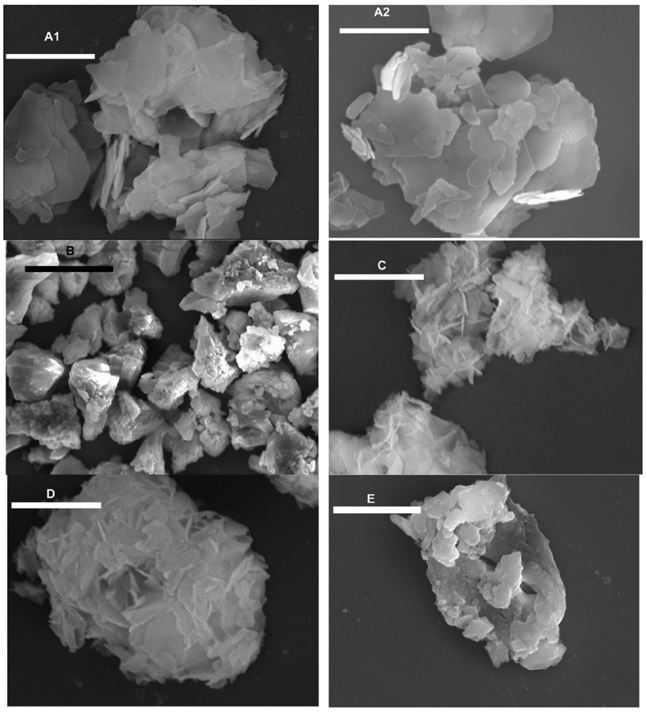

Figure 6. Scanning electron micrographs of some representative samples. A1 and A2, sample Ca2Al1; B, sample C-Ca2Al1; C, sample Eu1; D, sample Eu2Nd2; E, sample C-Eu2Nd4. Scale: bar corresponds to 10 μm.

Scanning electron micrographs of representative samples are shown in Figure 6. Primary lamellar particles are formed, with a large aspect ratio value, for hydrocalumite (Figure 6A1,A2). The average size of the particles is about 10 μm, and their widths around 2 μm, as easily concluded from observation of some particles oriented perpendicular to the sample holder. Upon calcination (C-Ca2Al1, Figure 6B) the particles are much more compact, probably because of water release and crystallographic phase transformation. This compaction would also account for the extremely low specific surface areas measured for the calcined

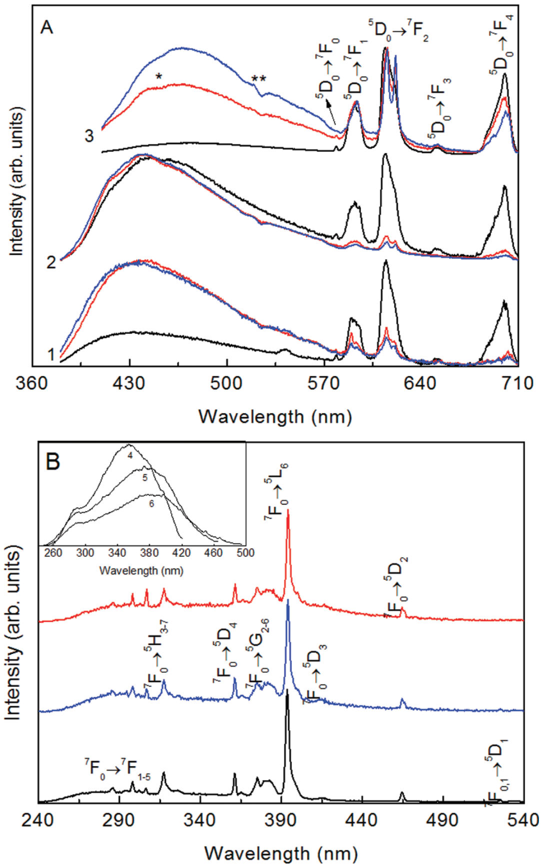

Figure 7. (A) Emission and (B) excitation spectra excited at (1) 270, (2) 360, and (3) 395 nm and monitored at 614 nm, respectively, for Eu2 (black line), Eu2Nd2 (red line), and Eu2Nd4 (blue line). (*) and (**) denote the intra-4f^3 $^4I_{9/2} \to {}^2K_{15/2}$, $^2G_{9/2,7/2}$ self-absorptions. The inset shows the excitation spectra monitored at (4) 440, (5) 480, and (6) 510 nm for Eu2.

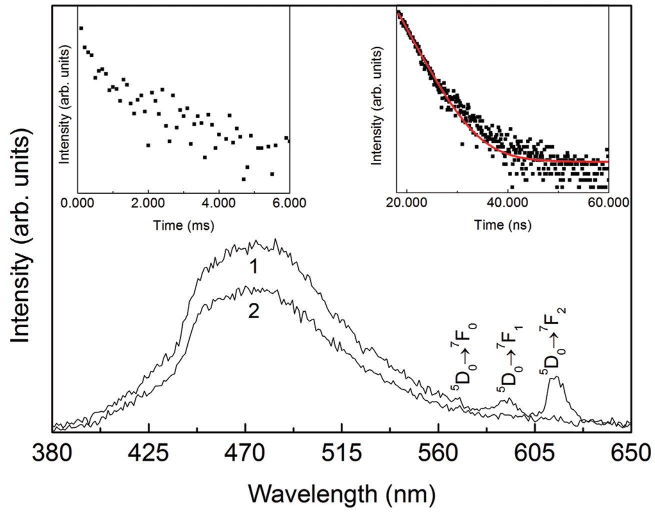

Figure 8. Time resolved emission spectra (10 K) excited at 330 nm acquired with SD values of (1) 0.05 ms and (2) 10.00 ms and an integration window of 20.00 ms. The insets show the emission decay curves plotted in a semilogarithmic y-axis scale monitored at 470 nm, excited at 330 nm, and acquired at (left) 10 K and (right) 300 K. The red line in the latter inset represents the data best fit using a single exponential function $I(t) = I_0 \exp(-(t - t_0)/\tau)$, where I_0 is the intensity at $t = t_0 = 18.40$ ns (reduced-$\chi^2 = 1.97 \times 10^{-4}$).

solids. The average particle sizes of the secondary particles and uncalcined samples are roughly the same, but the lamellar aspect disappears upon calcination.

Incorporation of Eu has an important impact on the morphology of the particles. Although primary lamellar particles are still identified, sample Eu1 in Figure 6C, now they are not stacked forming a layered structure, as for sample Ca2Al1, but appear forming sand-rose agglomerates, thus exposing a larger surface and probably accounting for the specific surface area development observed for this sample if compared to Ca2Al1 (see Table 4). This process is even more evident when Nd is added, sample Eu2Nd2, Figure 6D. In this case, the apparent size of the secondary particles is somewhat larger than in the former case, but also exposing a larger area. Calcination of the lanthanide-containing samples leads to stacking of the primary lamellar particles, losing the sand-rose aspect, sample C-Eu2Nd2, Figure 6E.

Photoluminescence. Figure 7A shows the emission features of the Eu^{3+}- and Eu^{3+}/Nd^{3+}-containing materials, prior to the thermal treatment, for different excitation wavelengths. The emission is formed by a series of lines ascribed to the Eu^{3+} $^5D_0 \to {}^7F_{0-4}$ transitions superimposed on a broad band, whose maximum intensity shifts toward the red as the excitation wavelength increases. The relative intensity of the intra-4f^6 lines and the broad band depend both on the excitation wavelength and on the amount of Ln^{3+} incorporated. The broad band emission dominates the spectra in the excitation wavelength range 270−395 nm, whereas at higher excitation wavelengths the relative intensity of the $^5D_0 \to {}^7F_{0-4}$ transitions increases. For the single Eu^{3+}-doped material (Eu2), the intra-4f^6 lines dominate the spectra in the entire excitation interval, and the relative intensity of the broad band increases for an excitation wavelength of ca. 360 nm. This dependence on the Ln^{3+} concentration and excitation wavelength indicates energy transfer processes involving the states associated with the broad band and the intra-4f levels. In order to gain some insight into the origin of such a broad band, time-resolved emission spectroscopy was performed for a selected sample (Eu2Nd2) at 10 K and room temperature, for distinct starting delay (SD) values under the excitation interval 330−390 nm. The emission spectrum excited at 10 K, for SD = 0.05 ms, reveals the presence of a broad band (380−650 nm) superimposed on the intra-4f^6 lines (Figure 8). Increasing the SD value to 10.00 ms, only the long-lived broad band could be detected. In order to estimate the respective lifetime value, the emission decay curve was monitored at 470 nm and excited at 330 nm. The emission decay reveals a non-single exponential behavior (left inset in Figure 8), so that an average lifetime value ($\langle\tau\rangle$) was estimated, considering $\langle\tau\rangle = (\int_{t_0}^{t_1} I(t)\, t\, dt)/(\int_{t_0}^{t_1} I(t)\, dt)$, where $t_0 = 0$ and t_1 is the time interval where the luminescence intensity ($I(t)$) reaches the background, yielding approximately 1.88 ± 0.05 ms. Such a time scale range (ms) ruled out the presence of Eu^{2+} related emission as it typically occurs with a faster decay rate (≈1 μs).[53] At room-temperature, the emission decay curves occur in a much faster time scale, with a lifetime value of 4.10 ± 0.03 ns. Moreover, a similar broad band emission (excited within almost the same energy range) was already reported for pure Co−Al-LDHs.[54] Although the nature of this emission remains unclear, we speculate that the band is due to Al-related defects.[55,56]

The emission spectra of the Eu^{3+}/Nd^{3+} codoped LDHs display intra-4f^3 self-absorptions (most evident for the material with higher Nd^{3+} content, Eu2Nd4) assigned to the $^4I_{9/2} \to {}^2K_{15/2}$, $^2G_{7/2}$ transitions. Such self-absorptions indicate the presence of radiative

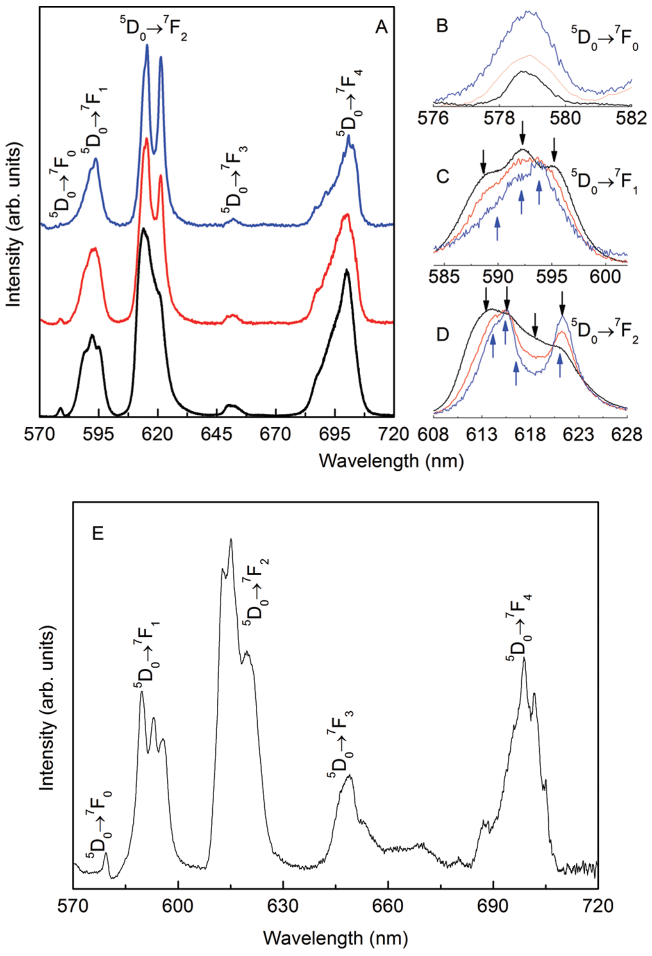

Figure 9. (A) High-resolution emission spectra, excited at 395 nm, for Eu2 (black line), Eu2Nd2 (red line), and Eu2Nd4 (blue line). (B), (C), and (D) show a magnification of the $^5D_0 \to {}^7F_{0-2}$ transitions, respectively. The $^5D_0 \to {}^7F_0$ emission for Eu2Nd2 and Eu2Nd4 was measured with 100 accumulation scans. (E) High-resolution emission spectra (10 K) excited at 395 nm for Eu2Nd4.

energy transfer, namely, part of the emitted visible light is absorbed by the Nd^{3+} cations, and subsequently converted into NIR emission, as discussed below. The radiative energy transfer has been previously observed and named the "inner filter" effect.[57]

The excitation spectra (Figure 7B) of Eu2, Eu2Nd2, and Eu2Nd4 monitored within the $^5D_0 \to {}^7F_2$ transition display intra-4f^6 lines, attributed to the $^7F_0 \to {}^7F_{1-5}$, $^5D_{4-1}$, $^5G_{2-6}$, and $^5L_6$ and $^7F_1 \to {}^5D_1$ transitions, and a faint broad emission centered at 280 nm, more evident after calcination (see below). The spectrum (inset in Figure 7B) monitored at 440 nm (within the broad emission band) exhibits a broad band with a main component at 355 nm and a low-intensity one at 290 nm and is similar to that reported for pure Co−Al-LDHs.[54] Increasing the monitoring wavelength to 510 nm, the former band broadens and shifts toward the red, whereas the energy of the low-wavelength components remains unaltered.

The Eu^{3+}-local structure was studied in detail by monitoring the $^5D_0 \to {}^7F_{0-4}$ transitions at higher resolution. Figure 9A shows the emission spectra for all the samples prior to the thermal treatment under the excitation wavelength that maximizes the Eu^{3+} emission intensity (395 nm, Figure 7B). All the spectra display the $^5D_0 \to {}^7F_0$ line and 3 and 4 Stark components of the $^5D_0 \to {}^7F_{1,2}$ transitions, respectively (Figures 9B−D). Moreover, for the Eu2Nd4 the emission spectrum measured at 10 K (Figure 9E) exhibits the same general profile with the $^5D_0 \to {}^7F_0$ line and the 3 and 4 components for the $^5D_0 \to {}^7F_{1-2}$ transitions, recorded without the need of any accumulation scans. The single $^5D_0 \to {}^7F_0$ line (whose energy is given in Table 5) and the J-degeneracy splitting of the $^7F_{1,2}$ levels into 3 and 4 Stark components, respectively, indicate that Eu^{3+} resides in a low-symmetry site. This low-symmetry site does not have an inversion center because the $^5D_0 \to {}^7F_2$ lines are more intense that the $^5D_0 \to {}^7F_1$ lines.[58]

Moreover, the emission features are independent of the excitation wavelength (not shown), supporting the presence of a single average local environment in the materials. Comparing the spectra of the Eu^{3+}-doped material with the spectra of the Eu^{3+}/Nd^{3+} doped samples, one finds that while the energy and fwhm of the Eu^{3+} Stark components remain essentially constant (in particular for $^5D_0 \to {}^7F_0$, Table 5), changes are apparent in their relative intensity (most evident for the $^5D_0 \to {}^7F_2$ transition), indicating that the incorporation of Nd^{3+} changes the Eu^{3+} neighborhood.

The $^5D_0$ emission decay curves were monitored within the $^5D_0 \to {}^7F_2$ transition under direct intra-4f^6 excitation ($^5L_6$, 395 nm). The emission decay curves of the samples prior to the thermal treatment are well described by a single exponential function yielding the lifetime values in Table 6. The presence of a single exponential behavior for the emission decay curves is in accord with the presence of a single Eu^{3+} local environment. The decrease in the $^5D_0$ lifetime value for the codoped samples (ca. 7%, Table 6) agrees with the changes reported above for the emission spectrum and indicates nonradiative deactivation channels, not present in the single doped Eu2. The $^5D_0$ lifetime value dependence on the incorporation of the Nd^{3+} ions can be further rationalized in terms of the $^5D_0$ quantum efficiency (η), $\eta = k_r/(k_r + k_{nr})$, where k_r and k_{nr} are the radiative and nonradiative transition probabilities, respectively, using a procedure based on the integrated areas of the $^5D_0 \to {}^7F_{0-4}$ emission lines and $^5D_0$ lifetime value, both recorded at room temperature.[36] As shown in Table 6, the quantum efficiency decreases from 0.045 to 0.039 after the Nd^{3+} incorporation, due to a slight decrease (ca. 5%) of the radiative transition probability and mainly due to an increase (ca. 10%) of the nonradiative transition probability. The fact that CEu2Nd2 and CEu2Nd4 have approximately the same η, k_r, and k_{nr} values indicates that in this Nd^{3+} concentration range the $^5D_0$ emission features are essentially the same.

In order to evaluate the potential of the Eu^{3+}- and Eu^{3+}/Nd^{3+}-doped LDHs to be used as photoluminescent ceramic pigments, a detailed study of the calcined samples was performed. Calcination has an impact on the local lanthanide environments of the samples and, therefore, changes are expected in the photoluminescent features. In particular, CaO contains a single Ca^{2+} crystallographic site and, thus, if Eu^{3+} substitutes for Ca^{2+} a single site is also expected. Mayenite contains two similar Ca^{2+} sites, but one of them has occupancy of ca. 90%. Hence, Eu^{3+} for Ca^{2+} substitution will generate, mainly, a single site. The emission spectra will reflect the presence of two Eu^{3+}-average local environments (attributed to Eu^{3+} sites in CaO and mayenite) in the calcined materials, as detailed below.

The CEu2, CEu2Nd2, and CEu2Nd4 are multiwavelength emitters in the UV/vis/NIR spectral regions. For excitation wavelengths between 270 and 360 nm, the UV/vis emission spectra (Figure 10A) consist of a large broad band shifted to the red (ca. 2550 cm^{-1}), by comparison with that observed prior to the thermal treatment (Figure 9A). For higher excitation

Table 5. Energy (E_{00}, cm^{-1}) and fwhm (fwhm$_{00}$, cm^{-1}) of the $^5D_0 \rightarrow {}^7F_0$ Transition Estimated for All the Materials

	Eu2	CEu2	Eu2Nd2	CEu2Nd2	Eu2Nd4	CEu2Nd4
E_{00}	17377.2 ± 0.3	17320.0 ± 0.8	17377.0 ± 0.8	17317.3.6 ± 1.6	17377.0.0 ± 1.2	17316.0 ± 1.8
fwhm$_{00}$	50.4 ± 0.7	36.7 ± 1.4	46.2 ± 0.8	55.0 ± 3.1	50.0 ± 2.1	55.0 ± 3.0
E_{00}		17375.0 ± 0.7		17373.5 ± 0.9		17372.7 ± 1.0
fwhm$_{00}$		38.2 ± 0.4		34.2 ± 1.5		34.3 ± 1.7

Table 6. $^5D_0$ Lifetime (τ, ms), Quantum Efficiency (η), and Radiative (k_r, ms^{-1}) and Non-Radiative (k_{nr}, ms^{-1}) Transition Probability Values for the Non-Calcined Materials Excited at 394 nm

	Eu2	Eu2Nd2	Eu2Nd4
τ	0.190 ± 0.001	0.175 ± 0.003	0.173 ± 0.004
k_r	0.236	0.224	0.229
k_{nr}	5.027	5.490	5.551
η	0.045	0.039	0.039

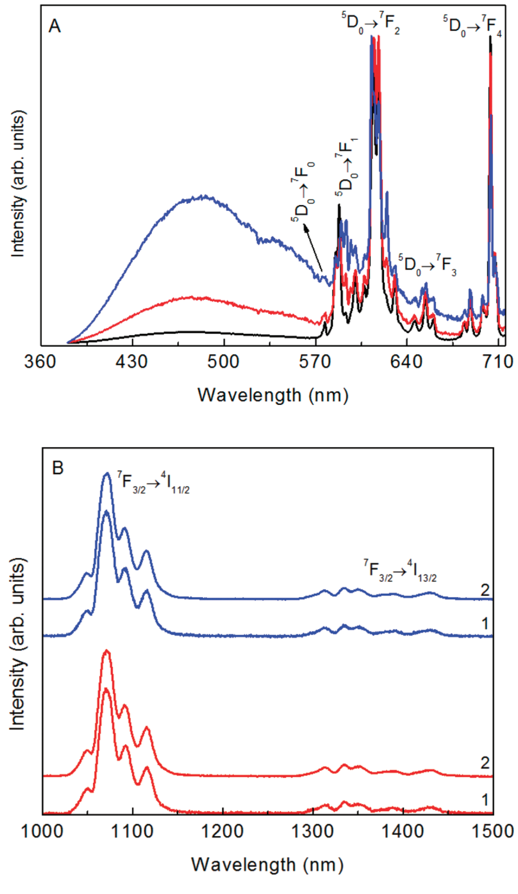

Figure 10. (A) UV/vis emission spectra for CEu2 (black line), CEu2Nd2 (red line), and CEu2Nd4 (blue line) excited at 270 nm and (B) NIR emission spectra of CEu2Nd2 (red line) and CEu2Nd4 (blue line) excited at (1) 287 and (2) 524 nm.

wavelengths (360−395 nm), only the intra-4f^6 lines are detected, with no sign of the broad band (not shown). Figure 10B shows the NIR emission spectra ascribed to the intra-4f^3 transitions. We note that for the nontreated materials (Eu2Nd2 and Eu2Nd4), no room temperature NIR emission could be detected, indicating that the thermal treatment contributed to decrease the nonradiative paths for the Nd^{3+} excited levels (OH oscillators are absent from the Nd^{3+}-local environments of the CaO and mayenite phases).

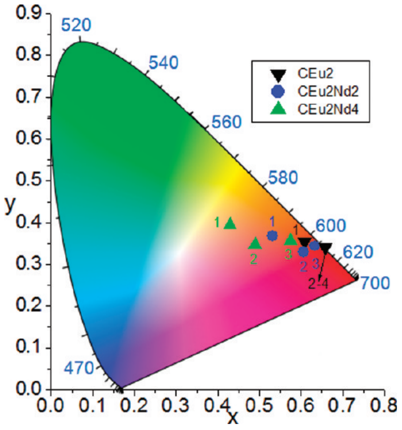

Figure 11. CIE chromaticity diagram showing the (x,y) emission color coordinates of the calcined materials at different excitation wavelengths: (1) 280 nm, (2) 360 nm, (3) 394 nm, (4) 465 nm, and (5) 532 nm.

The photoluminescence features of the calcined LDH materials were quantified through the estimation of the absolute emission quantum yields. The maximum value, 0.06, was obtained for the CEu2 sample under excitation at 270 nm. For the remaining samples (both the noncalcined and the codoped ones), the absolute quantum yield values lie below the detection limits of our equipment (0.01). Those results point out that the (i) thermal treatment has an important role in the enhancement of the photoluminescence features and (ii) codoping favors the appearance of nonradiative mechanisms both for the broad band component and the Eu^{3+} emission.

The potential of the calcined materials to be used as ceramic pigments is further evidenced by the estimation of the emission color coordinates as function of the excitation wavelength and Nd^{3+} concentration (Figure 11). The emission color coordinates of the pure Eu^{3+}-calcined material can be tuned within the reddish-orange spectral region, from (0.61,0.35) to (0.64,0.34) by varying the excitation wavelength from 280 to 394 nm. For the material with lower Nd^{3+}-content (CEu2Nd2) the emission color varies from orange-pink (0.53,0.36) to reddish-orange (0.63,0.34) crossing the pink region (0.61,0.33) in the same excitation interval. A wider emission color variation is observed with CEu2Nd4 material, varying from the white central part of the diagram (0.43,0.39) to the orange-pink (0.49,0.35) and reddish-orange (0.575,0.356) regions excited at 280, 360, and 394 nm, respectively. Under selective intra-4f^6 excitation at 465 and 532 nm all the calcined materials exhibit pure red color emission (0.66,0.34). For simplicity, those color coordinates are only shown in the diagram of Figure 11 for the CEu2.

The contribution to the emission spectrum of the calcined samples of the Eu^{3+} local environments of the CaO and mayenite was ascertained via high-resolution emission and selective excitation spectra. Figure 12 shows the high-resolution emission

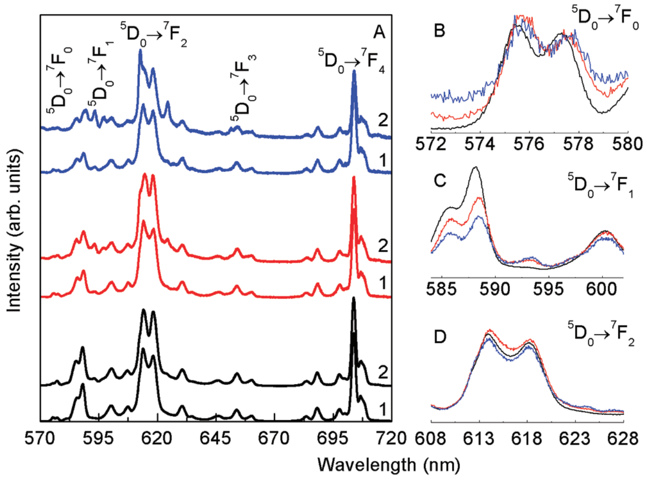

Figure 12. (A) Room temperature emission spectra excited at (1) 394 and (2) 280 nm for Eu2 (black line), Eu2Nd2 (red line), and Eu2Nd4 (blue line). (B), (C), and (D) show a magnification of the $^5D_0 \rightarrow {}^7F_{0-2}$ transitions, respectively.

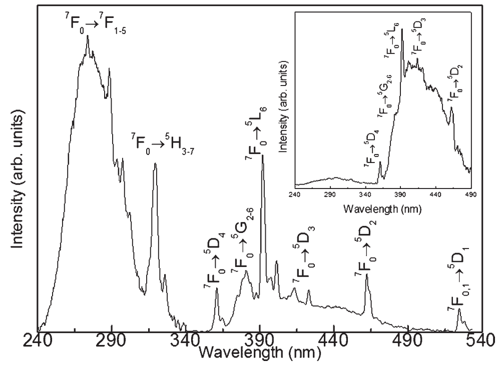

Figure 13. Excitation spectrum of the CEu2 monitored at 577.6 nm. The inset shows the excitation spectrum monitored at 573.3 nm.

spectra for all the calcined samples at two excitation wavelengths. The presence of two lines for the $^5D_0 \rightarrow {}^7F_0$ transition, the J-degeneracy splitting of the $^7F_{1,2}$ levels in more than 3 and 5 Stark components, respectively, indicates that the Eu^{3+} ions are present in, at least, two distinct local environments. Moreover, the emission features strongly depend on the excitation wavelength, in good agreement with the presence of, at least, two distinct Eu^{3+} local environments. The energy and fwhm of the two lines ascribed to the $^5D_0 \rightarrow {}^7F_0$ transition were calculated assuming a sum of two Gaussian functions (Table 5). The excitation spectra were selectively monitored within the two $^5D_0 \rightarrow {}^7F_0$ transitions at 573.3 and 577.6 nm, Figure 13. The former excitation spectrum monitored at high energy (573.3 nm) consists of a band at 425 nm and a series of low-relative-intensity intra-$4f^6$ lines. The spectrum monitored at low-energy (577.6 nm) reveals the presence of a main broad band at 280 nm superimposed on a series of intra-$4f^6$ lines. The former resembles the band observed in Eu^{3+}-doped CaO which has been ascribed to a ligand-to-metal charge transfer (LMCT) state.[59] Therefore, we tentatively ascribe the low-energy $^5D_0 \rightarrow {}^7F_0$ transition (17320.0 ± 0.8 cm^{-1}, Table 5) to the Eu^{3+} substituting for Ca^{2+} in the CaO phase and the high-energy $^5D_0 \rightarrow {}^7F_0$ transition (17375.0 ± 0.7 cm^{-1}, Table 5) to Eu^{3+} replacing the high-occupancy Ca^{2+} site in mayenite.

Table 7. $^5D_0$ **Lifetime Values (τ, ms) for the Calcined Materials Excited at 394 nm**

	CEu2	CEu2Nd2	CEu2Nd4
τ	0.119 ± 0.004	0.115 ± 0.005	0.012 ± 0.001
	0.736 ± 0.041	0.760 ± 0.018	0.284 ± 0.010

The emission decay curves of the calcined samples reveal a biexponential behavior, consistent with the presence of two different Eu^{3+}-containing phases, yielding the lifetimes collected in Table 7. Moreover, the $^5D_0$ lifetime value of the Eu^{3+}-CaO local environment is larger than the one assigned to the Eu^{3+}-mayenite local site and similar to the values reported for the low-symmetry local environments of Eu^{3+} centers in CaO.[59]

We note that Nd^{3+} may also be present in the CaO and mayenite phases. Nevertheless, the electronic structure of the intra-$4f^3$ levels (in particular the absence of a transition between nondegenerated states) renders the determination of selective emission and excitation spectra difficult. Therefore, the excitation spectra monitored on the $^4F_{3/2} \rightarrow {}^4I_{11/2}$ transition for CEu2Nd2 and CEu2Nd4 (inset of Figure 10B) display a series of intra-$4f^3$ lines and a broad band at ca. 287 nm, ascribed to Al-related defects, shifted to the red relative to the band measured in the excitation spectra of Eu2 (Figure 7B). The higher intensity of the intra-$4f^3$ lines relative to the broad band indicates that the Nd^{3+} ions are mainly populated via direct intra-4f excitation.

■ CONCLUSIONS

Lanthanide (Eu and Nd)-doped hydrocalumite has been prepared by a coprecipitation method. All samples, with Eu and Nd contents up to 4% (molar ratio), show a single crystalline phase, with segregation of no secondary lanthanide-containing phases, and suggesting isomorphical substitution in the lattice of hydrocalumite. Upon calcination, mayenite and lime are formed; while for lime the lattice parameters coincide with those reported in the literature, small differences are observed for the mayenite phase. However, layered crystals are formed, which collapse to compact crystals upon calcination.

The photoluminescence spectra of the noncalcined samples consist of intra-4f transitions and a broad band ascribed to Al-related defects. Energy transfer from these defect states to the Eu^{3+} and Nd^{3+} ions was clearly discerned. The codoped Eu^{3+}/Nd^{3+} materials are the first example of vis/NIR multiwavelength emitter LDHs covering almost the entire visible range and part of the NIR spectral region. In all the samples, the Eu^{3+} ions occupy a single, low symmetry site without an inversion center. The $^5D_0$ lifetime values and quantum efficiency of the codoped LDHs decrease ca. 10% relatively to those of the single-Ln doped material, suggesting that incorporation of Nd^{3+} activates nonradiative channels for the $^5D_0$ depopulation. The as-prepared samples were calcined to evaluate the potential of the Eu^{3+}- and Eu^{3+}/Nd^{3+}-doped LDHs to be used as photoluminescent ceramic pigments. Under excitation at 270 nm, the sample doped only with Eu^{3+} exhibits an absolute emission quantum yield of 0.06. The emission color coordinates of the pure Eu^{3+}-calcined material can be tuned within the reddish-orange spectral region, by varying the excitation wavelength from 280 to 394 nm. For the codoped materials, and the same excitation range, the emission color varies from the white central part of the diagram to the orange-pink and reddish-orange, depending on the Nd^{3+} concentration. The emission spectra of the calcined samples provide evidence for two Eu^{3+} local environments, attributed to Eu^{3+} sites in CaO and mayenite. The Eu^{3+}-CaO phase is essentially excited through a

LMCT band (at ca. 280 nm) and is characterized by a low-energy $^5D_0 \rightarrow {}^7F_0$ line and a larger $^5D_0$ lifetime value, relatively to the energy of the same transition and to the lifetime value in Eu^{3+}-mayenite. The apparent discrepancy between the PXRD (lattice parameter of the CaO identical to the value reported in the literature, suggesting that this phase results undoped) and luminescence (two environments for Eu^{3+}, in mayenite and in CaO) results may arise from a larger sensitivity of luminescence properties of Eu^{3+} in different environments, than that of PXRD to minor modifications in the chemical composition of CaO by Eu^{3+} doping.

In summary, high-temperature stable ceramic pigments, prepared from Eu^{3+} and Nd^{3+} doped LDH precursors, afford multiwavelength luminescent materials emitting in a large vis/NIR spectral region, with potential applications as barcodes and in broadband amplifiers.

AUTHOR INFORMATION

Corresponding Author

*Tel.: +34923294489. Fax: +34923294574. E-mail: vrives@usal.es.

ACKNOWLEDGMENT

M.E.P.-B., R.J.R.-C., and V.R. acknowledge financial support from MICINN (Grant MAT2009-08526), Junta de Castilla y León (Grant SA111A09), and ERDF. R.A.S.F., L.D.C., and J.R. thank FCT and FEDER for financial support.

REFERENCES

(1) Cavani, F.; Trifirò, F.; Vaccari, A. *Catal. Today* **1991**, *11*, 173.

(2) Trifirò, F.; Vaccari, A. Hydrotalcite-like anionic clays (Layered double hydroxides). In *Comprehensive Supramolecular Chemistry*; Atwood, J. L., Davies, J. E. D., MacNicol, D. D., Vögtle, F., Lehn, J.-M., Eds.; Pergamon: Oxford, U.K., 1996; Vol. 7, pp 251−291.

(3) Vaccari, A. *Catal. Today* **1998**, *41*, 53.

(4) Rives, V.; Ulibarri, M. A. *Coord. Chem. Rev.* **1999**, *181*, 61.

(5) Rives, V., Ed. *Layered Double Hydroxides: Present and Future*; Nova Sci. Pub. Inc.: New York, 2001.

(6) Wypych, F., Satyanarayana, K. G., Eds. *Clay Surfaces: Fundamentals and Applications*; Elsevier: Amsterdam, 2004.

(7) Rives, V. *Mater. Chem. Phys.* **2005**, *75*, 19.

(8) Duan, X.; Evans, D. G. *Layered Double Hydroxides*; Springer: Berlin, 2006.

(9) Bergaya, F., Theng B., K. G., Lagaly, G., Eds. *Handbook of Clay Science*; Elsevier: Amsterdam, 2006.

(10) Basile, F.; Vaccari, A. Applications of Hydrotalcite-type Anionic Clays (Layered Double Hydroxides) in Catalysis. In *Layered Double Hydroxides: Present and Future*; Rives, V., Ed.; Nova Sci. Pub. Inc.: New York, 2001; pp 285−321.

(11) Monzón, A.; Romeo, E.; Marchi, A. J. Hydrogenation Catalysts by Mixed Oxides prepared from LDH. In *Layered Double Hydroxides: Present and Future*; Rives, V., Ed.; Nova Sci. Pub. Inc.: New York, 2001; pp 323−382.

(12) Rives, V.; Labajos, F. M.; Trujillano, R.; Romeo, E.; Royo, C.; Monzón, A. *Appl. Clay Sci.* **1998**, *13*, 363.

(13) Rives, V.; Prieto, O.; Dubey, A.; Kannan, S. *J. Catal.* **2003**, *220*, 161.

(14) Costantino, U.; Nocchetti, M. Layered Double Hydroxides and their Intercalation Compounds in Photochemistry and in Medicinal Chemistry. In *Layered Double Hydroxides: Present and Future*; Rives, V., Ed.; Nova Sci. Pub. Inc.: New York, 2001; pp 383−411.

(15) Del Arco, M.; Cebadera, E.; Gutiérrez, S.; Martín, C.; Montero, M. J.; Rives, V. J.; Rocha, M. A.; Sevilla *J. Pharm. Sci.* **2004**, *93*, 1649.

(16) Del Arco, M.; Gutiérrez, S.; Martín, C.; Rives, V.; Rocha, J. *J. Solid State Chem.* **2004**, *177*, 3954.

(17) Carriazo, D.; Del Arco, M.; Fernández, A.; Martín, C.; Rives, V. *J. Pharm. Sci.* **2010**, *99*, 3372.

(18) Kovanda, F.; Kovácsová, E.; Kolousek, D. *Collect. Czech. Chem. Commun.* **1999**, *64*, 1517.

(19) Ulibarri, M. A.; Hermosín, M. C. Layered Double Hydroxides in Water Decontamination. In *Layered Double Hydroxides: Present and Future*; Rives, V., Ed.; Nova Sci. Pub. Inc.: New York, 2001; pp 251−284.

(20) Taviot-Gueho, C.; Leroux, F. In situ Polymerization and Intercalation of Polymers in Layered Double Hydroxides. In *Layered Double Hydroxides*; Duan, X., Evans, D. G., Eds.; Springer: Berlin, 2006; pp 121−159.

(21) Herrero, M.; Benito, P.; Labajos, F. M.; Rives, V.; Zhu, Y. D.; Allen, G. C.; Adams, J. M. *J. Solid State Chem.* **2010**, *183*, 1645.

(22) Jaubertie, C.; Holgado, M. J.; San Román, M. S.; Rives, V. *Chem. Mater.* **2006**, *18*, 3114.

(23) Nebot-Díaz, I. Ph. D. Thesis, Universitat Jaume I, Castelló, Spain, 2001.

(24) Ruano-Casero, R. J.; Pérez-Bernal, M. E.; Rives, V. *Z. Anorg. Allgm. Chem.* **2005**, *631*, 2142.

(25) García-García, J. M.; Pérez-Bernal, M. E.; Ruano-Casero, R. J.; Rives, V. *Solid State Sci.* **2007**, *9*, 1115.

(26) Pérez-Bernal, M. E.; Ruano-Casero, R. J.; Benito, F.; Rives, V. *J. Solid State Chem.* **2009**, *182*, 1593.

(27) Pérez-Bernal, M. E.; Ruano-Casero, R. J.; Rives, V. *J. Solid State Chem.* **2009**, *182*, 2566.

(28) Li, C.; Wang, G.; Evans, D. G.; Duan, X. *J. Solid State Chem.* **2004**, *177*, 4569.

(29) Gago, S.; Pillinger, M.; Sá Ferreira, R. A.; Carlos, L. D.; Santos, T. M.; Gonçalves, I. S. *Chem. Mater.* **2005**, *17*, 5803.

(30) Li, C.; Wang, L.; Evans, D. G.; Duan, X. *Ind. Eng. Chem. Res.* **2009**, *48*, 2162.

(31) Fernández, J. M.; Barriga, C.; Ulibarri, M. A.; Labajos, F. M.; Rives, V. *Chem. Mater.* **1997**, *9*, 312.

(32) Gunawan, P.; Wu, R. *J. Phys. Chem. C* **2009**, *113*, 17206.

(33) Musumeci, A. W.; Xu, Z. P.; Smith, S. V.; Minchin, R. F.; Martin, D. J. *J. Nanopart. Res.* **2010**, *12*, 111.

(34) Poudret, L.; Prior, T. J.; McIntyre, L. J.; Fogg, A. M. *Chem. Mater.* **2008**, *20*, 7447.

(35) Zhu, Q.; Li, J.-G.; Zhi, C.; Li, X.; Sun, X.; Sakka, Y.; Golberg, D.; Bando, Y. *Chem. Mater.* **2010**, *22*, 4204.

(36) Carlos, L. D.; Ferreira, R. A. S.; De Zea Bermudez, V.; Ribeiro, S. J. L. *Adv. Mater.* **2009**, *21*, 509.

(37) Rousselot, I.; Taviot-Gueho, C.; Leroux, F.; Léone, P.; Palvadeau, P.; Besse, J. P. *J. Solid State Chem.* **2002**, *167*, 137.

(38) Iwata, T.; Haniud, M.; Fukuda, K. *J. Solid State Chem.* **2008**, *181*, 51.

(39) Campos-Molina, M. L.; Santamaría-González, J.; Mérida-Robles, J.; Moreno-Tost, R.; Alburquerque, M. C. G.; Bruque-Gámez, S.; Rodríguez-Castellón, E.; Jiménez-López, A.; Maireles-Torres, P. *Energy Fuels* **2010**, *24*, 979.

(40) Kim, S.-W.; Matsuishi, S.; Miyakawa, M.; Hayashi, K.; Hirano, M.; Hosono, M. *J. Mater. Sci., Mater. Electron* **2007**, *18*, 55.

(41) Palacios, L.; Cabeza, A.; Bruque, S.; García-Granda, S.; Asande, M. A. G. *Inorg. Chem.* **2008**, *47*, 2661.

(42) Lim, Y. T.; Noh, Y.-W.; Cho, J.-H.; Han, J. H.; Choi, B. S.; Kwon, J.; Hong, K. S.; Gokarna, A.; Cho, Y.-H.; Chung, B. H. *J. Am. Chem. Soc.* **2009**, *131*, 17145.

(43) Ishii, N.; Teisset, C. Y.; Fuji, T.; Kohler, S.; Schmid, K.; Veisz, L.; Baltuska, A.; Krausz, F. *IEEE J. Sel. Top. Quantum Electron* **2006**, *12*, 173.

(44) Rodríguez-Carvajal, J. *Program of Structure Fitting, AFFMA*, PC version, 1990.

(45) Gay, P. *The Crystalline State, an Introduction*; Oliver & Boyd: Edinburgh, 1972.

(46) Moore, D. M.; Reynolds, R. C., Jr. *X-Ray Diffraction and the Identification and Analysis of Clay Minerals*; OUP: Oxford, 1989.

(47) Bastida, J.; Bolós, C.; Pardo, P.; Serrano, F. J. *Bol. Soc. Esp. Ceram. Vidrio* **2004**, *43*, 80.

(48) Waddington, T. C. *Adv. Inorg. Chem. Radiochem.* **1959**, *1*, 180.

(49) Kloprogge, J. T.; Frost, R. L. Infrared and Raman Spectroscopic Studies of Layered Double Hydroxides. In *Layered Double Hydroxides: Present and Future*; Rives, V., Ed.; Nova Sci. Pub. Inc.: New York, 2001; pp 139−192.

(50) Kloprogge, J. T. Infrared and Raman Spectroscopy of Naturally Occurring Hydrotalcites and Their Synthetic Equivalents. In *The application of vibrational spectroscopy to clay minerals and layered double hydroxides*; Kloprogge, J. T., Ed.; CMS Workshop Lectures; The Clay Mineral Society: Aurora, CO, 2005; Vol. 13, pp 204−238.

(51) Rives, V. *Adsorpt. Sci. Technol.* **1991**, *8*, 95.

(52) Lippens, B. C.; De Boer, J. H. *J. Catal.* **1965**, *4*, 319.

(53) Yamashita, N. *J. Electrochem. Soc.* **1993**, *140*, 840.

(54) Sun, S.; Guo Hou, W. *Chin. Chem. Lett.* **2007**, *18*, 1371.

(55) Yoshino, K.; Mikami, H.; Imai, K.; Yoneta, M.; Ikari, T. *Phys. B: Condens. Matter* **2001**, *302−303*, 299.

(56) Ando, M.; Kanemitsu, Y.; Kushida, T.; Matsuda, K.; Salki, T.; White, C. W. *Appl. Phys. Lett.* **2001**, *79*, 539.

(57) Molina, C.; Ferreira, R. A. S.; Poirier, G.; Fu, L.; Ribeiro, S. J. L.; Messsaddeq, Y.; Carlos, L. D. *J. Phys. Chem. C* **2008**, *112*, 19346.

(58) Carlos, L. D.; Videira, A. L. L. *Phys. Rev. B* **1994**, *49*, 11721.

(59) Van der Voort, D.; Imhof, A.; Blasse, G. *J. Solid State Chem.* **1992**, *96*, 311.